


## Article

# Metal–Organic Framework-Derived Mn/Ni Dual-Metal Single-Atom Catalyst for Efficient Oxygen Reduction Reaction

Zewen Sun <sup>1,2</sup>, Siyuan Zhang <sup>2</sup>, Bo Zheng <sup>2</sup>, Yue Zhou <sup>2</sup>, Wenshu Chen <sup>2</sup>, Rui Liu <sup>1,\*</sup> , Guangxiang Liu <sup>2,\*</sup> and Leiming Lang <sup>2,\*</sup>

<sup>1</sup> School of Chemistry and Molecular Engineering, Nanjing Tech University, Nanjing 211816, China

<sup>2</sup> Laboratory of Advanced Functional Materials of Nanjing, Nanjing Xiaozhuang University, Nanjing 211171, China

\* Correspondence: rui.liu@njtech.edu.cn (R.L.); njuliugx@126.com (G.L.); langleiming@njzcu.edu.cn (L.L.)

**Abstract:** Non-precious-metal-based oxygen reduction reaction (ORR) catalysts hold great prospects for rechargeable metal–air batteries and reversible electrolyzer/fuel cell systems. Among the various earth-abundant and noble-metal-free catalysts, Mn- and Ni-based single-atom catalysts (SACs) are attracting attention for ORRs. Herein, we designed a facile and efficient strategy to obtain Mn/Ni dual-metal single-atom catalysts, in which atomic Mn and Ni sites were dispersed on nitrogen-doped porous carbon. The optimized Mn/Ni catalysts showed excellent ORR electrocatalytic performance with a half-wave potential of 0.803 V, comparable to that of commercial Pt/C catalysts. Meanwhile, the electron transfer number was determined to be 3.9, indicating a good four-electron reaction process. The excellent electrocatalytic performance was attributed to the N-doped porous carbon structure with a large specific surface area, which afforded abundant active sites to anchor the single Mn and Ni atoms.

**Keywords:** oxygen reduction; electrocatalysts; Mn/Ni dual-metal single atom; N-doped



**Citation:** Sun, Z.; Zhang, S.; Zheng, B.; Zhou, Y.; Chen, W.; Liu, R.; Liu, G.; Lang, L. Metal–Organic Framework-Derived Mn/Ni Dual-Metal Single-Atom Catalyst for Efficient Oxygen Reduction Reaction. *Inorganics* **2023**, *11*, 101. <https://doi.org/10.3390/inorganics11030101>

Academic Editors: Jincheng Li, Shichao Ding, Zhaoyuan Lyu and Xin Li

Received: 19 January 2023

Revised: 21 February 2023

Accepted: 27 February 2023

Published: 28 February 2023



**Copyright:** © 2023 by the authors. Licensee MDPI, Basel, Switzerland. This article is an open access article distributed under the terms and conditions of the Creative Commons Attribution (CC BY) license (<https://creativecommons.org/licenses/by/4.0/>).

## 1. Introduction

The energy crisis and environmental pollution have greatly limited the progress of human society, raising an urgent demand for the development of sustainable, clean, green energy and energy storage equipment. In this respect, new energy batteries such as fuel cells with high energy density and low pollution show convincing prospects [1]. However, due to the sluggish reaction kinetics of the cathodic oxygen reduction reaction (ORR), the working efficiency and output performance of the battery are obviously reduced [2–9]. Noble-metal-based catalysts with excellent performance are widely used to accelerate the ORR process on the cathode of fuel cells [10–14]. However, the disadvantages of high price, rare source reserves, and low anti-poisoning capability have greatly limited their large-scale application [15–18]. To overcome these issues, low-cost, high-activity and high-stability non-noble metal catalysts are expected.

Single-atom catalysts (SACs), especially transition metal–nitrogen–carbon (MNC) [19–23], have been widely studied in the electrocatalyzed ORR due to their excellent atomic utilization, small size effect, highly unsaturated coordination environment, high intrinsic activity and favorable interaction between metal and substrates [24–26]. In recent years, Cr-, Fe-, Co-, Ni-, Cu-, and Zn-based SAC materials have been developed for ORR. Among them, Fe-N-C catalysts with Fe-N<sub>x</sub> active sites showed the most superior catalytic performance [27–33]. However, one serious issue of Fe-based catalysts is their poor durability [34,35]. The two-electron reduction of the hydrogen peroxide intermediate of the ORR could trigger the Fenton reaction at Fe active sites, generating strong-oxidizing radicals, which damage the material's structure and deteriorate the overall performance [36]. Different from the Fe-N-C catalyst, the Mn-N-C counterpart exhibits low reactivity for the Fenton reaction

and is hardly affected by hydrogen peroxide [37–40]. Meanwhile, previously reported thermodynamic and kinetic theoretical calculation results [37–40] have also shown that Mn-N-C catalysts have a comparable catalytic performance to that of Fe-N-C. On the other hand, Ni-N-C coordination sites have been proven to exhibit excellent ORR activity and stability [41]. Recently, dual-metal single-atom catalysts (DMSACs) were designed to optimize and improve the catalytic performance of the ORR because of the unique advantage of SACs and the synergistic interaction between two adjacent metal atoms [42–46]. In view of the above, the coexistence of two different Mn and Ni SA sites in N-doped carbon may enhance the ORR performance through pairing and/or long-range coupling, altering each other's coordination environment and electronic structure [47,48].

Metal–organic framework (MOF)-derived porous carbon materials have drawn extensive attention as promising electrocatalysts owing to their high specific surface areas, porous structure and good electron conductivity. MOFs are convenient to prepare using cheap Fe, Co, Ni and Mn salts as the starting materials, and can be employed as a template to construct different porous carbons and their composites by a one-step pyrolytic process [17,19,20,27,35,36,49]. Recently, many MOF-derived metal–nitrogen–carbon SACs have been obtained. Peng's group reported the synthesis of metal SACs using metal-based MOFs (Fe, Co, Ni) with nanocube structures obtained by a co-precipitating method [17]. Liu's group investigated a Mn SAC prepared by the one-step thermal activation of the precursor  $\text{Mn}(\text{CH}_3\text{COO})_2@ZIF-8$  [27]. Yao et al. synthesized a Ni SAC by the direct carbonization of the Ni–MOF with a subsequent etching and activation process [49]. Among them, imidazole, the isocyano group and amino acids were often used as ligands to prepare complex precursors. Otherwise, the 2,2'-bipyridine (Bpy) is also a good candidate because of the simple molecule structure, rich nitrogen content, low cost and rare report.

Herein, a Mn/Ni dual-metal single-atom catalyst was synthesized by the simple carbonization of the Mn/Ni 2,2'-bipyridine (Bpy) complex precursor and an acid-rinsing process. The formed porous N-doped carbon substrate provided abundant active sites to construct an atomically dispersed Mn and Ni single-atom microstructure. The prepared Mn/Ni DMSAC showed better electrocatalytic activity than the prepared MnNC and NiNC single-atom catalysts and presented an overpotential and half-wave potential comparable to the Pt/C catalyst.

## 2. Results

The synthetic route of the manganese–nickel dual-metal single-atom porous carbon catalyst is shown in Figure 1. The complex MnNi-Bpy precursors were directly synthesized by the co-precipitation method using 2,2-bipyridine, nickel and manganese salts as the starting materials. MNNC-x catalysts were obtained by carbonizing the above precursor in a  $\text{N}_2$  atmosphere at 800 °C for 1 h at different heating rates, followed by washing with acid and deionized water and a drying process (synthesis details in the experimental section). Thermogravimetric (TG) analysis was carried out to display the conversion process from the complex precursor to MNNC-2. Three obvious weight-loss stages were observed from the TG results of the as-synthesized products (Figure S1). The first mass loss appeared before 250 °C, which was ascribed to the evaporation of 2,2-bipyridine and ethanol. The following obvious weight loss between 300 °C and 500 °C was attributed to the decomposition and carbonization of the MnNi-Bpy-2. The further crystallization of the product took place between 800 °C and 900 °C. When the temperature was higher than 900 °C, no weight loss was observed, indicating the complete carbonization of the precursor to MNNC-2.

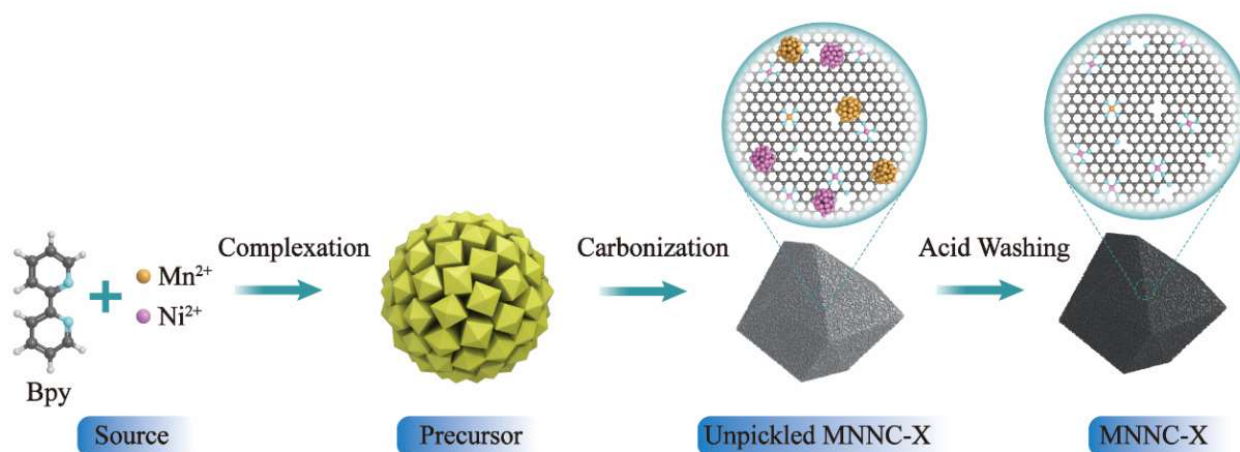


**Figure 1.** Schematic diagram for the synthesis of MNNC.

X-ray diffraction (XRD) analysis was used to determine the chemical composition and crystal structure of the sample. The XRD pattern of MNNC-2 (Figure 2a) showed obvious broad peaks at about  $25^\circ$  and  $44^\circ$ , which were attributed to the characteristic diffraction peaks of carbon (002) and (100) [10]. No characteristic peaks related to Mn-based or Ni-based crystal species were detected, suggesting that no Mn-based or Ni-based crystal were found in the samples. In addition, MnNC exhibited a similar result to MNNC-2 (Figure S2), while NiNC showed three distinct peaks of nickel metal and one broad peak of carbon (Figure S3). The morphology of MNNC-2 was observed by field emission scanning electron microscopy and transmission electron microscopy (FE-SEM and TEM). In the SEM images (Figure S4), the MnNi-Bpy-2 precursor appeared as a cluster of regular prisms. The Ni-Bpy precursor (Figure S4c) was composed of some particles, which were smaller than that of Mn-Bpy (Figure S4d). The morphological difference may be attributed to the various synthetic conditions. Only a small Ni-Bpy complex can be obtained under the same reaction condition as that of Mn-Bpy. Therefore, the MnNi-Bpy-2 precursor displayed a similar morphology to that of Mn-Bpy, where the main composition was Mn-Bpy. MNNC-2 presented a blocky shape (Figure 2b,c), which was ascribed to the structure change during calcination. As displayed in the TEM image (Figure 2d), it showed a large number of dense micropores, and no nanoparticles or clusters could be found. In addition, the corresponding element mapping in Figure 2e reflected the uniform distribution of C, N, Mn and Ni elements. By contrast, for the unpickled MNNC-2 (Figure S5), there were a lot of nanoparticles with clear lattice fringes, which could be assigned to the Ni or Mn metal. For a more precise observation, an aberration-corrected high-angle annular dark-field scanning transmission electron microscope (AC HAADF-STEM, Figure 2f) revealed a large number of scattered bright white spots. Combined with the above characterizations, it was speculated that these bright spots came from the atomically dispersed Mn and Ni components, which were substantially embedded in the N-doped carbon skeleton and beneficial to the improvement of ORR performance [3,7,10,11,19,30].

To determine the surface chemical configurations of MNNC-2, X-ray photoelectron spectroscopy (XPS) spectra were recorded. The total metal content within MNNC-2 was 0.61% as obtained by XPS peak data. The mass contents of Mn and Ni were 0.41% and 0.2%. The high-resolution Mn 2p XPS spectrum for MNNC-2 (Figure 3a) displayed the binding energies of Mn  $2p_{3/2}$  (641.4 eV) and Mn  $2p_{1/2}$  (653.4 eV) along with a satellite peak at 645.3 eV, which were attributed to the characteristics of  $Mn^{2+}$  [19]. The Mn 3s XPS spectrum (Figure S6) also demonstrated the existence of  $Mn^{2+}$  because of the 5.9 eV banding difference between two peaks (82.5 eV and 88.4 eV). Similarly, the deconvolution results of the Ni 2p XPS (Figure 3b) showed that there were two main peaks at 856.1 and 873.7 eV, which were ascribed to the  $2p_{3/2}$  and  $2p_{1/2}$  of the  $Ni^{2+}$  species, respectively [26]. Additionally, the two broad peaks at 861.4 and 880.4 eV were identified as shake-up

satellites of Ni 2p<sub>3/2</sub> and Ni 2p<sub>1/2</sub>, respectively. The type of N dopant in MNNC-2 sample was also analyzed (Figure 3c). It was deconvoluted into five configurations assigned to pyridinic N (398.4 eV), pyrrolic-N (400.9 eV), metal-N<sub>x</sub> species (399.1 eV), graphitic N (401.4 eV) and oxidized N (403.8 eV) [10,11]. The peaks at 284.8, 285.9, and 289.6 eV for the C 1s spectra (Figure S7) were ascribed to C=C, C-N and C-O, respectively. In the Raman spectra (Figure 3d), the I<sub>D</sub>/I<sub>G</sub> values of MnNC, NiNC and MNNC-2 carbonized at 800 °C were 1.100, 1.168 and 1.185, respectively. This indicated that MNNC-2 possessed slightly greater defects than the single-metal materials, which may have been helpful to the promotion of ORR performance. At the same time, we also investigated the effects of the raw material ratio and carbonization temperature on the graphitization degree and defective structure (Figures S8 and S9). The result showed that MNNC-2 presented more defective structures on the carbon materials.

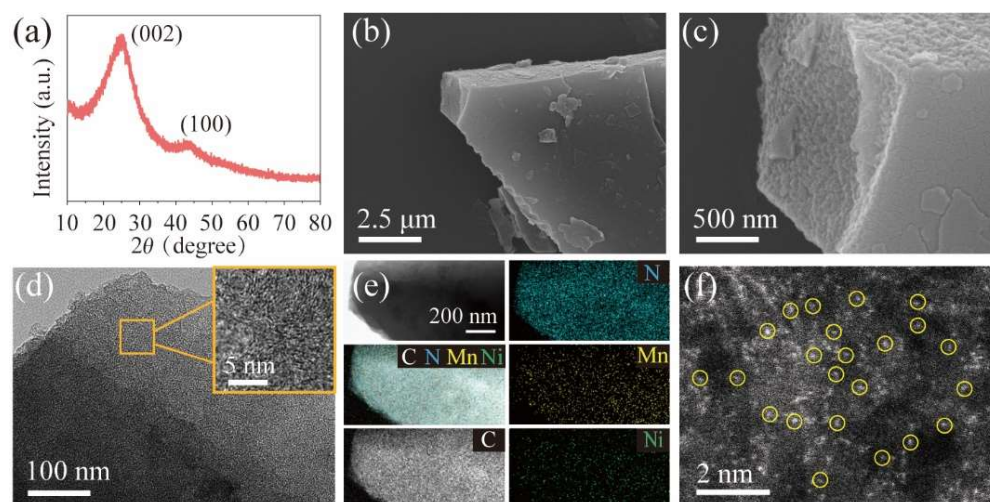


**Figure 2.** (a) XRD pattern, (b,c) SEM images, (d) TEM images, (e) EDS mapping for C, N, Mn, and Ni elements, (f) AC HAADF-STEM image of MNNC-2.

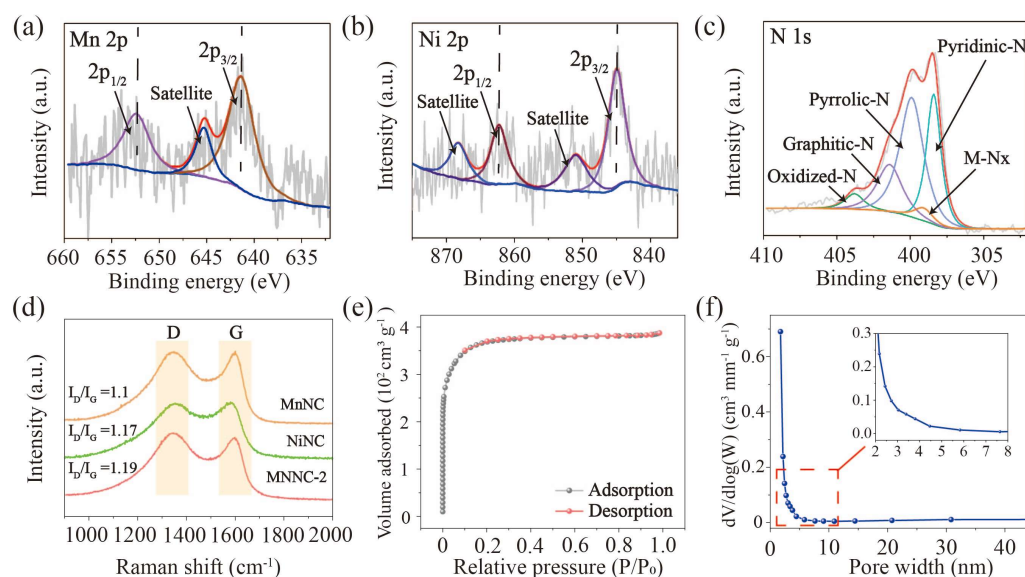


**Figure 3.** (a) Mn 2p, (b) Ni 2p and (c) N 1s XPS spectra for MNNC-2. (d) Raman spectra of MnNC, NiNC and MNNC-2. (e) N<sub>2</sub> adsorption–desorption isotherms and (f) the corresponding pore size distribution curve for MNNC-2.



Furthermore, the specific surface area of MNNC-2 was up to  $1408 \text{ m}^2 \text{ g}^{-1}$  in the  $\text{N}_2$  adsorption–desorption test (Figure 3e), which attributed to the abundant pore structure after calcination. The pore size distribution curve (Figure 3f) showed the existence of affluent micropores in MNNC-2. However, the relatively low specific area of MnNC ( $130 \text{ m}^2 \text{ g}^{-1}$ ) and NiNC ( $7 \text{ m}^2 \text{ g}^{-1}$ ) (Figure S10a,b) attributed to the few micropores (Figure S10c,d). The large specific surface area and rich pore structure of MNNC-2 can not only provide more active sites, but also facilitate mass transfer during the ORR, leading to a stronger kinetic process. Additionally, MNNC-1 and MNNC-3 had similar  $\text{N}_2$  adsorption–desorption isotherms and corresponding pore size distribution plots to MNNC-2. The results indicated that the three samples with different feeding ratios of raw materials had similar specific surface areas and pore size distributions.

In order to attain a highly active catalyst, the control experiments were investigated regarding the carbonization temperature, heating rate and Mn/Ni mole ratio. The ORR activity testing of different samples in  $\text{O}_2$ -saturated alkaline (0.1 M KOH) electrolyte was conducted. The half-wave potentials of the samples carbonized at  $700 \text{ }^\circ\text{C}$  and  $900 \text{ }^\circ\text{C}$  were  $0.708 \text{ V}$  and  $0.79 \text{ V}$ , respectively (Figure 4), which was lower than that of MNNC-2 carbonized at  $800 \text{ }^\circ\text{C}$ . The samples attained at higher heating rates showed low electrocatalytic activity of  $E_{1/2} = 0.791 \text{ V}$  for  $5 \text{ }^\circ\text{C}/\text{min}^{-1}$  and  $E_{1/2} = 0.787 \text{ V}$  for  $10 \text{ }^\circ\text{C}/\text{min}^{-1}$  (Figure 5), which proved that the low heating rate of  $2 \text{ }^\circ\text{C}/\text{min}^{-1}$  can maintain the micropore structure during calcination. The feed mole ratios of the Mn and Ni salts also had an influence on the ORR performance. MNNC-2 (Mn:Ni = 1) exhibited better activity than the other samples MNNC-1 (Mn:Ni = 1:7) and MNNC-3 (Mn:Ni = 7:1) (Figure 6). The optimum conditions were a 1:1 mole ratio of Mn and Ni,  $2 \text{ }^\circ\text{C}/\text{min}^{-1}$  heating rate and  $800 \text{ }^\circ\text{C}$  calcination temperature.

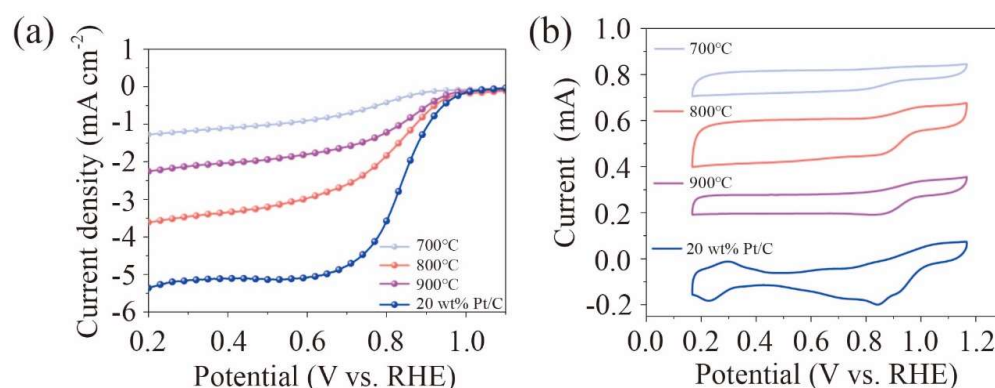


**Figure 4.** (a) RDE LSVs and (b) CVs of 20 wt.% Pt/C and MNNC-2 with different carbonization temperatures at a heating rate of  $2 \text{ }^\circ\text{C}/\text{min}^{-1}$  measured in  $\text{O}_2$ -saturated 0.1 M KOH and at a scan rate of  $10 \text{ mV s}^{-1}$ . The rotation speed for LSV test was 1600 rpm.

Further investigation of the MNNC-2 electrocatalytic performance was conducted. The CV curves for MNNC-2 in  $\text{O}_2$ - or  $\text{N}_2$ -saturated 0.1 M KOH (Figure S12) showed that an obvious reduction peak appeared in the  $\text{O}_2$ -saturated electrolyte, indicating that MNNC-2 had remarkable ORR catalytic activity. The linear sweep voltammetry (LSV) polarization curves (Figure 7a) showed that MNNC-2 exhibited a higher onset potential ( $E_{\text{onset}} = 0.981 \text{ V}$ ) and half-wave potential ( $E_{1/2} = 0.803 \text{ V}$ ), which were better than those of the single-metal atomic catalysts MnNC ( $E_{\text{onset}} = 0.958 \text{ V}$ ,  $E_{1/2} = 0.653 \text{ V}$ ) and NiNC ( $E_{\text{onset}} = 0.758 \text{ V}$ ,  $E_{1/2} = 0.602 \text{ V}$ ), indicating that the synergistic effect of the Mn and Ni dual-metal single atom enhanced the ORR performance. Meanwhile, MNNC-2 ( $3.606 \text{ mA}\cdot\text{cm}^{-2}$ ) exhibited a higher limiting current density than MnNC ( $2.25 \text{ mA}\cdot\text{cm}^{-2}$ ) and NiNC ( $1.68 \text{ mA}\cdot\text{cm}^{-2}$ ), indicating that it had a higher mass transfer efficiency. Figure 7b shows that the Tafel slope of MNNC-2 is  $135.77 \text{ mV dec}^{-1}$ , which was lower than that of MnNC ( $148.46 \text{ mV dec}^{-1}$ ) and higher than that of the Pt/C catalyst ( $116.01 \text{ mV dec}^{-1}$ ). In addition, the ORR pathway

of MNNC-2 was confirmed by rotating ring-disk electrode (RRDE) measurements. The  $\text{HO}_2^-$  yield was maintained below 5%, and the electron transfer number  $n$  of MNNC-2 was calculated to be 3.89 (Figure 7c), indicating an effective four-electron transfer process. The CV curve of MNNC-2 also exhibited a more positive reduction peak potential than the Pt/C catalyst (Figure 7e). After 800 cycles of CV measurements in 0.1 M KOH solution, MNNC-2 indicated good electrochemical stability without a change in onset potential and only a decrease of 36 mV for half-wave potential (Figure 7f).

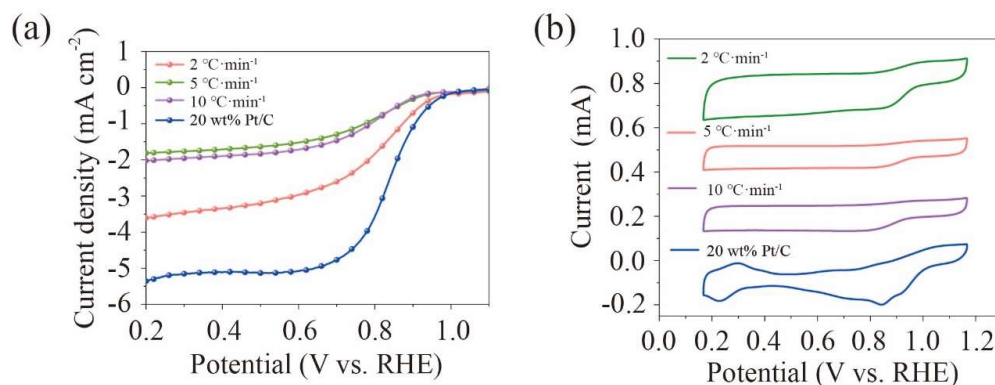


**Figure 5.** (a) RDE LSVs and (b) CVs of 20 wt.% Pt/C and MNNC-2 with different heating rates of 2 °C min<sup>-1</sup>, 5 °C min<sup>-1</sup> and 10 °C min<sup>-1</sup> measured in O<sub>2</sub>-saturated 0.1 M KOH at a scan rate of 10 mV s<sup>-1</sup>. The rotation speed for LSV test was 1600 rpm.

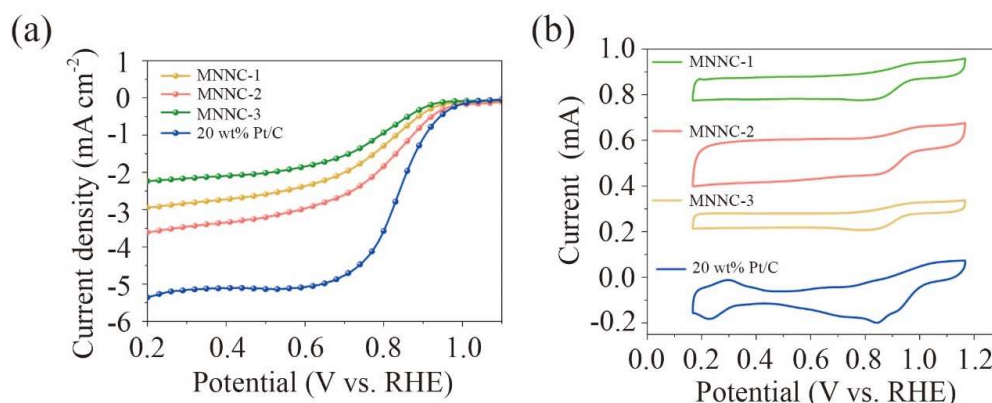


**Figure 6.** (a) RDE LSVs and (b) CVs of MNNC-1, MNNC-2, MNNC-3 and 20 wt.% Pt/C in O<sub>2</sub>-saturated 0.1 M KOH at a scan rate of 10 mV s<sup>-1</sup>. The rotation speed for LSV test was 1600 rpm.

Electrochemical impedance spectroscopy (EIS) measurements were conducted to qualitatively compare the charge transfer resistance ( $R_{ct}$ ) of the MnNC, NiNC, and MNNC-2 catalysts. The results are presented as Nyquist plots ( $Z'$  vs.  $-Z''$ ), where  $Z'$  and  $Z''$  refer to the real and imaginary parts of electrode impedance, respectively. The typical characteristics of the two Nyquist plots are one semicircle in the high-frequency range and a sloping straight line in the low-frequency range. An intercept at the  $Z'$  axis at a high frequency corresponds to the resistance of the electrolytes. The  $R_{ct}$  of NiNC was estimated to be 74.69  $\Omega$  according to the Nyquist plots (Figure S13), which was smaller than that of MnNC (113.89  $\Omega$ ) and MNNC-2 (107.20  $\Omega$ ). The low  $R_{ct}$  of NiNC could be ascribed to the existence of Ni crystal in porous carbon, which promoted the conductivity of the catalyst. The radius of the semicircles of MNNC-2 was smaller than that of the MnNC electrode (Figure S12) because of the incorporation of single-atom Ni. These results demonstrated that MNNC-2 had an optimized ORR catalytic activity after introducing single Ni atoms to the MnNC catalyst.

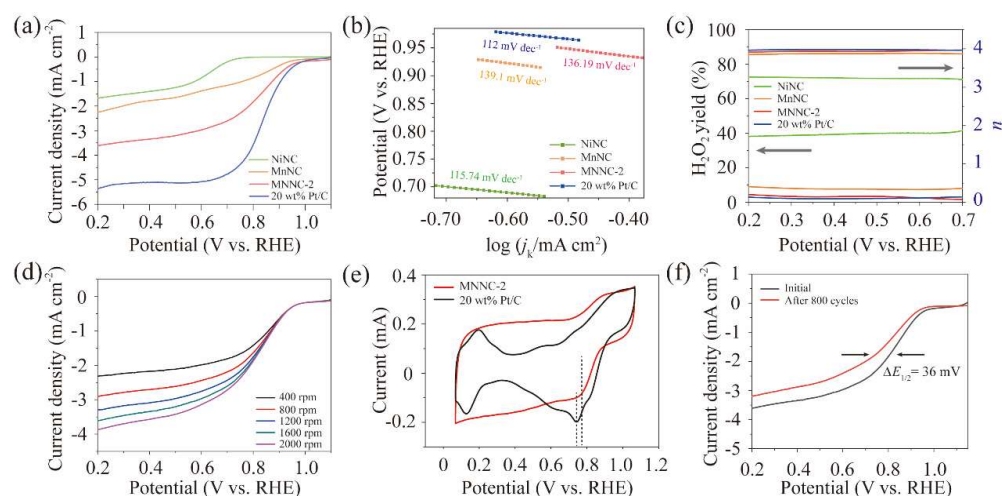


**Figure 7.** (a) LSV polarization curves and (b) Tafel plots of MnNC, NiNC, MNNC-2 and Pt/C measured at 1600 rpm in O<sub>2</sub>-saturated 0.1 M KOH. (c) Electron transfer number *n* (right) and H<sub>2</sub>O<sub>2</sub> yield (left) vs. potential for MNNC-2 and Pt/C derived from the RRDE tests. (d) LSV curves of MnNC, NiNC, MNNC-2 recorded at different rotation speeds recorded in O<sub>2</sub>-saturated 0.1 M KOH. (e) The CV curves for MNNC-2 and 20 wt.% Pt/C catalysts at the scan rate of 10 mV s<sup>-1</sup> in O<sub>2</sub>-saturated 0.1 M KOH. (f) The stability curves of MNNC-2.

Compared with commercial Pt/C catalysts, MNNC-2 exhibited a slightly low ORR electrocatalytic activity. The possible reason was that MNNC-2 suffered from numerous microporous architectures, which severely limited the diffusion coefficient of the reactants and prevented the accessibility to the interior active sites. Moreover, the large size of the MNNC-2 particle was not beneficial to the regular dispersal of the catalyst on the surface of the electrode, which also had an influence on the electron transfer efficiency and current density. Further study of the electrocatalytic activity improvement will be carried out in our future research work.

### 3. Materials and Methods

#### 3.1. Chemical Reagents and Materials

Nickel chloride hexahydrate (NiCl<sub>2</sub>·6H<sub>2</sub>O, AR), manganese chloride tetrahydrate (MnCl<sub>2</sub>·4H<sub>2</sub>O, AR) and anhydrous ethanol were obtained from Sinopharm. 2,2'-bipyridine (Bpy, AR) was obtained from Sinopharm. High-purity nitrogen (99.999%), high-purity oxygen (99.999%) and high-purity argon (99.999%) were obtained from Tianhong Qiti. All the chemicals were used without further purification.

#### 3.2. Preparation of Mn-Bpy Precursor

MnCl<sub>2</sub>·4H<sub>2</sub>O (1.28 mmol, 0.253 g) was added to 8 mL of ethanol to generate solution A. Subsequently, solution B was formed by dissolving 2,2'-bipyridine (Bpy, 10.24 mmol, 1.6 g) in 8 mL of ethanol. After that, solution B was poured slowly into solution A and agitated for 24 h at ambient temperature [19]. The finally obtained light-yellow precipitates were centrifuged, washed several times with a small amount ethanol, and dried overnight under vacuum at 60 °C.

#### 3.3. Preparation of Ni-Bpy Precursor

NiCl<sub>2</sub>·6H<sub>2</sub>O (1.28 mmol, 0.304 g) was added into 8 mL of ethanol to generate solution A. Then, solution B was formed by dissolving 2,2'-bipyridine (Bpy, 2.24 mmol, 0.35g) and TEA (0.0875 mL) in 3.5 mL of ethanol. Solution B was slowly added to solution A with a plastic tip dropper. While rapidly stirring the solution, a small amount of solid was gradually precipitated and agitated for 24 h at ambient temperature [26,27]. The finally

obtained light-green precipitates were centrifuged, washed several times with a small amount ethanol, and dried overnight under vacuum at 60 °C.

#### 3.4. Preparation of MnNi-Bpy Precursor

MnCl<sub>2</sub>·4H<sub>2</sub>O (1.6 mmol, 0.316 g) and NiCl<sub>2</sub>·6H<sub>2</sub>O (1.6 mmol, 0.38 g) were added into 20 mL of ethanol to generate solution A. Subsequently, solution B was formed by dissolving 12.8 mmol of 2,2'-bipyridine (Bpy) in 20 mL of methanol. After that, solution B was rapidly poured into solution A and agitated for 24 h at ambient temperature. The finally obtained bright-yellow precipitates were centrifuged, washed several times with a small amount of ethanol, and dried overnight under vacuum at 60 °C. The different MnNi-Bpy precursors were prepared by altering the feed mole ratio of Mn and Ni salts and named MnNi-Bpy-1 (Mn:Ni = 1:7), MnNi-Bpy-2 (Mn:Ni = 1) and MnNi-Bpy-3 (Mn:Ni = 7:1) [19,27].

#### 3.5. Preparation of MnNC, NiNC, MNNC-1, MNNC-2 and MNNC-3

The different catalysts of the single Mn and Ni atoms anchored in N-doped carbon (MnNC, NiNC, MNNC-2) were obtained by the carbonization of Mn-Bpy, Ni-Bpy and MnNi-Bpy-2 (Mn:Ni = 1) precursors under N<sub>2</sub> flow at 800 °C for 1 h, with a heating rate of 2 °C·min<sup>-1</sup> and subsequent rinsing in 2 mol·L<sup>-1</sup> H<sub>2</sub>SO<sub>4</sub>, washed with water and dried overnight under vacuum at 60 °C. MNNC-1 and MNNC-3 were attained by using the same synthetic method as MNNC-2 except using the MnNi-Bpy-1 (Mn:Ni = 1:7) and MnNi-Bpy-3 (Mn:Ni = 7:1) precursors, respectively.

#### 3.6. Preparation of Contrast Samples

The contrast samples were obtained by using similar methods as for MNNC-2 except the carbonization temperature and heating rate. The MNNC-700 and MNNC-900 catalysts were synthesized by using the MnNi-Bpy-2 (Mn:Ni = 1) complex as a precursor, with a heating rate of 2 °C·min<sup>-1</sup>, under N<sub>2</sub> flow at 700 °C and 900 °C for 1 h, respectively. The contrast catalysts were also obtained by using the same synthetic method as MNNC-2, except using the different heating rates of 2 °C·min<sup>-1</sup>, 5 °C·min<sup>-1</sup> and 10 °C·min<sup>-1</sup>, respectively.

#### 3.7. Characterization

The composition of the sample was characterized by an Empyrean X-ray diffractometer (XRD, Rigaku D/max-2200PC), in which Cu K $\alpha$  rays ( $\lambda = 0.154$  nm) were used. The tube voltage was 40 kV, the tube current was 50 mA, and the scanning speed was 2 min<sup>-1</sup>. A Japan Hitachi 7200 comprehensive thermal analyzer was used, and the thermal stability of the precursor sample was analyzed. The morphology and structure of all the samples were characterized by a scanning electron microscope (SEM, Hitachi Regulus8100) operated at 5 kV and a transmission electron microscope (TEM) and HRTEM (JEOL JEM 2100F) operated at 200 kV. The spherical-aberration-corrected TEM image was collected using an FEI Themis Z operated at 300 kV. The specific surface area and pore size distribution were characterized by the Micromeritics 3Flex type analyzer of Micromeritics, USA. Before the test, the sample was vacuum-dried at 100 °C for 12 h, and then degassed at 200 °C for 12 h. The nitrogen absorption and desorption curves were measured under 77 K liquid nitrogen. The X-ray photoelectron spectroscopy (XPS) was recorded on a K-Alpha spectrometer (Thermo Scientific, Waltham, MA, USA). The Raman spectrometer was obtained from in Via-Reflex, England (532 nm excitation wavelength).

#### 3.8. Electrochemical Measurements

Electrochemical measurements were carried out at room temperature on a CHI 760E electrochemical workstation in a standard three-electrode system. The working electrode was a rotating ring-disk electrode (RRDE, 0.247 cm<sup>2</sup>). In 0.1 M KOH solution, the reference electrode and counter electrode was an Ag/AgCl electrode (saturated KCl aqueous solution) and a graphite sheet rod, respectively. For modifying the RRDE, 24  $\mu$ L of the catalysts' ink with a concentration of 4 mg mL<sup>-1</sup>, which was dispersed by sonication in a 1 mL



mixed solution of water (0.246 mL) and isopropanol (0.75 mL) containing 40  $\mu\text{L}$  Nafion, was pipetted onto the fresh RRDE surface, respectively. Cyclic voltammetry (CV) curves and LSV polarizations were acquired in Ar- or  $\text{O}_2$ -saturated 0.1 M KOH solution. All the measured potentials were converted to the RHE scale. The hydrogen peroxide yield and  $n$  were calculated by rotating ring-disk electrode (RRDE) measurements.

The hydrogen peroxide yield ( $\text{H}_2\text{O}_2$  %) and the electron transfer number ( $n$ ) were determined by the following equations:

$$\text{H}_2\text{O}_2(\%) = 200 \times \frac{I_r}{I_d + \frac{I_r}{N}}$$
$$n = 4 \times \frac{I_d}{I_d + \frac{I_r}{N}}$$

where  $I_d$  is disk current,  $I_r$  is ring current, and  $N$  is current collection efficiency of the Pt ring ( $N = 0.37$ ).

#### 4. Conclusions

In summary, we designed a Mn and Ni dual-metal single atom anchored in a N-doped porous carbon catalyst by using the N-rich MnNi-Bpy complex precursors and a calcination, rinsing, washing, and drying process. The contrast experiments were carried out to obtain the optimum synthetic conditions in terms of the metal/salt mole ratio (Mn:Ni = 1), heating rate ( $2\text{ }^\circ\text{C}\cdot\text{min}^{-1}$ ) and calcination temperature ( $800\text{ }^\circ\text{C}$ ). The Mn and Ni single-metal catalysts were also investigated by using a similar synthetic method to that of MNNC-2, except using different complex precursors. The characterizations of XRD, TEM mapping and HAADF-STEM illustrated the existence of single Mn and Ni atoms and a uniform dispersal on the carbon substrate. The electrocatalytic activity of different prepared catalysts was studied, which showed that introducing single Ni atoms enhanced the ORR performance of the Mn single-atom catalyst effectively. The optimized MNNC-2 displayed good electrocatalytic activity with a high onset potential and half-wave potential (0.803V), close to those of the commercial Pt/C catalyst. The prepared catalyst also demonstrated good electrochemical stability with little decrease in half-wave potential and without the loss of onset potential after 800 CV cycles. The good ORR performance of MNNC-2 was attributed to the N-rich porous carbon structure and the synergetic effect of the single Mn and Ni atoms. Furthermore, this green, simple, low-cost synthetic method provides an available guideline to attain highly effective non-noble metal electrocatalysts.

**Supplementary Materials:** The following supporting information can be downloaded at: <https://www.mdpi.com/article/10.3390/inorganics11030101/s1>, Figures S1: TGA plots of MnNi-Bpy-2, Figure S2: XRD pattern of MnNC, Figure S3: XRD pattern of NiNC, Figure S4: SEM images of (a, b) MnNi-Bpy-2, (c) Ni-Bpy and (d) Mn-Bpy, Figure S5: TEM images of MNNC-2 without acid washing, Figure S6: High-resolution Mn 3s XPS spectra of MNNC-2, Figure S7: High-resolution C 1s XPS spectra of MNNC-2, Figure S8: Raman spectra of MNNC-1, MNNC-2 and MNNC-3, Figure S9: Raman spectra of MNNC-2 carbonized at  $700\text{ }^\circ\text{C}$ ,  $800\text{ }^\circ\text{C}$  and  $900\text{ }^\circ\text{C}$ , Figure S10:  $\text{N}_2$  adsorption-desorption isotherms and corresponding pore size distribution plots of MnNC (a and c) and NiNC (b and d), Figure S11:  $\text{N}_2$  adsorption-desorption isotherms and corresponding pore size distribution plots of MNNC-1 (a and c) and MNNC-3 (b and d), Figure S12: CV curves for MNNC-2 in  $\text{O}_2$ - or  $\text{N}_2$ -saturated 0.1 M KOH at a scan rate of  $10\text{ mV s}^{-1}$ , Figure S13: Nyquist plots of MnNC, NiNC and MNNC-2 catalysts.

**Author Contributions:** Conceptualization, R.L. and L.L.; methodology, Z.S.; software, S.Z.; validation, Z.S., B.Z. and Y.Z.; formal analysis, W.C. and G.L.; investigation, Z.S.; resources, L.L., Y.Z. and G.L.; data curation, Z.S.; writing—original draft preparation, Z.S.; writing—review and editing, B.Z., Y.Z. and L.L.; supervision, R.L. and L.L.; project administration, G.L. and L.L.; funding acquisition, L.L. and Y.Z. All authors have read and agreed to the published version of the manuscript.

**Funding:** This research was funded by National Natural Science Foundation of China (No. 22004070) and Postgraduate Research & Practice Innovation Program of Jiangsu Province (No. XSJXC21\_72).

**Data Availability Statement:** Not applicable.

**Conflicts of Interest:** The authors declare no conflict of interest.

## References

1. Gao, L.; Xiao, M.; Jin, Z.; Liu, C.; Zhu, J.; Ge, J.; Xing, W. Correlating Fe Source with Fe-N-C Active Site Construction: Guidance for Rational Design of High-Performance ORR Catalyst. *J. Energy Chem.* **2018**, *27*, 1668–1673. [[CrossRef](#)]
2. Debe, M.K. Electrocatalyst Approaches and Challenges for Automotive Fuel Cells. *Nature* **2012**, *486*, 43–51. [[CrossRef](#)]
3. Lu, F.; Fan, K.; Cui, L.; Yang, Y.; Wang, W.; Zhang, G.; Wang, C.; Zhang, Q.; Li, B.; Zong, L.; et al. Cu-N<sub>4</sub> Single Atoms Derived from Metal-Organic Frameworks with Trapped Nitrogen-Rich Molecules and Their use as Efficient Electrocatalysts for Oxygen Reduction Reaction. *Chem. Eng. J.* **2022**, *431*, 133242. [[CrossRef](#)]
4. Wang, Z.L.; Xu, D.; Xu, J.J.; Zhang, X.B. Oxygen Electrocatalysts in Metal-air Batteries: From Aqueous to Nonaqueous Electrolytes. *Chem. Soc. Rev.* **2014**, *43*, 7746–7786. [[CrossRef](#)]
5. Cao, R.; Lee, J.-S.; Liu, M.; Cho, J. Non-Precious Catalysts: Recent Progress in Non-Precious Catalysts for Metal-Air Batteries. *Adv. Energy Mater.* **2012**, *2*, 701. [[CrossRef](#)]
6. Cheng, F.; Chen, J. Metal-Air Batteries: From Oxygen Reduction Electrochemistry to Cathode Catalysts. *Chem. Soc. Rev.* **2012**, *41*, 2172–2192. [[CrossRef](#)] [[PubMed](#)]
7. Yu, D.; Ma, Y.; Hu, F.; Lin, C.C.; Li, L.; Chen, H.Y.; Han, X.; Peng, S. Dual-Sites Coordination Engineering of Single Atom Catalysts for Flexible Metal–Air Batteries. *Adv. Energy Mater.* **2021**, *11*, 2100219. [[CrossRef](#)]
8. Ma, S.; Yuan, G.; Zhang, Y.; Yang, N.; Li, Y.; Chen, Q. Development of Encapsulation Strategies Towards the Commercialization of Perovskite Solar Cells. *Energy Environ. Sci.* **2022**, *15*, 13–55. [[CrossRef](#)]
9. Lin, Z.; Xiao, B.; Wang, Z.; Tao, W.; Shen, S.; Huang, L.; Zhang, J.; Meng, F.; Zhang, Q.; Gu, L.; et al. Planar-Coordination PdSe<sub>2</sub> Nanosheets as Highly Active Electrocatalyst for Hydrogen Evolution Reaction. *Adv. Funct. Mater.* **2021**, *31*, 2102321. [[CrossRef](#)]
10. Jiang, R.; Li, L.; Sheng, T.; Hu, G.; Chen, Y.; Wang, L. Edge-Site Engineering of Atomically Dispersed Fe-N<sub>4</sub> by Selective C-N Bond Cleavage for Enhanced Oxygen Reduction Reaction Activities. *J. Am. Chem. Soc.* **2018**, *140*, 11594–11598. [[CrossRef](#)]
11. Wu, H.; Wu, J.; Li, Y.; Li, W.; Zhai, J.; Jiang, Q.; Xu, X.; Gao, Y. Enhanced Oxygen Reduction with Carbon-Polyhedron-Supported Discrete Cobalt-Nitrogen Sites for Zn-Air Batteries. *Chem. Eng. J.* **2022**, *431*, 134084. [[CrossRef](#)]
12. Faraji, M.; Dehaghi, S.M. Pd-Doped g-C<sub>3</sub>N<sub>4</sub> Decorated by Nitrogen-Doped Carbon Quantum Dot as a High Performance Electrocatalyst with Superior Durability and Methanol Tolerance for Oxygen Reduction Reaction. *Inorg. Chem. Commun.* **2021**, *123*, 108328. [[CrossRef](#)]
13. Marković, N.M.; Schmidt, T.J.; Stamenković, V.; Ross, P.N. Oxygen Reduction Reaction on Pt and Pt Bimetallic Surfaces: A Selective Review. *Fuel Cells* **2001**, *1*, 105–116. [[CrossRef](#)]
14. Nie, Y.; Li, L.; Wei, Z. Recent Advancements in Pt and Pt-Free Catalysts for Oxygen Reduction Reaction. *Chem. Soc. Rev.* **2015**, *44*, 2168–2201. [[CrossRef](#)]
15. Dai, L.; Xue, Y.; Qu, L.; Choi, H.J.; Baek, J.B. Metal-Free Catalysts for Oxygen Reduction Reaction. *Chem. Rev.* **2015**, *115*, 4823–4892. [[CrossRef](#)]
16. Wang, Y.J.; Zhao, N.; Fang, B.; Li, H.; Bi, X.T.; Wang, H. Carbon-Supported Pt-Based Alloy Electrocatalysts for the Oxygen Reduction Reaction in Polymer Electrolyte Membrane Fuel Cells: Particle Size, Shape, and Composition Manipulation and Their Impact to Activity. *Chem. Rev.* **2015**, *115*, 3433–3467. [[CrossRef](#)] [[PubMed](#)]
17. Huang, H.; Yu, D.; Hu, F.; Huang, S.C.; Song, J.; Chen, H.Y.; Li, L.L.; Peng, S. Clusters Induced Electron Redistribution to Tune Oxygen Reduction Activity of Transition Metal Single-Atom for Metal-Air Batteries. *Angew. Chem. Int. Ed.* **2022**, *61*, e202116068.
18. Ma, S.; Deng, J.; Xu, Y.; Tao, W.; Wang, X.; Lin, Z.; Zhang, Q.; Gu, L.; Zhong, W. Pollen-Like Self-Supported FeIr Alloy for Improved Hydrogen Evolution Reaction in Acid Electrolyte. *J. Energy Chem.* **2022**, *66*, 560–565. [[CrossRef](#)]
19. Shang, H.; Sun, W.; Sui, R.; Pei, J.; Zheng, L.; Dong, J.; Jiang, Z.; Zhou, D.; Zhuang, Z.; Chen, W.; et al. Engineering Isolated Mn-N<sub>2</sub>C<sub>2</sub> Atomic Interface Sites for Efficient Bifunctional Oxygen Reduction and Evolution Reaction. *Nano Lett.* **2020**, *20*, 5443–5450. [[CrossRef](#)]
20. Wang, H.F.; Chen, L.; Pang, H.; Kaskel, S.; Xu, Q. MOF-Derived Electrocatalysts for Oxygen Reduction, Oxygen Evolution and Hydrogen Evolution Reactions. *Chem. Soc. Rev.* **2020**, *49*, 1414–1448. [[CrossRef](#)]
21. Xu, H.; Cheng, D.; Cao, D.; Zeng, X.C. A Universal Principle for A Rational Design of Single-Atom Electrocatalysts. *Nat. Catal.* **2018**, *1*, 339–348. [[CrossRef](#)]
22. Ling, C.; Shi, L.; Ouyang, Y.; Zeng, X.C.; Wang, J. Nanosheet Supported Single-Metal Atom Bifunctional Catalyst for Overall Water Splitting. *Nano Lett.* **2017**, *17*, 5133–5139. [[CrossRef](#)] [[PubMed](#)]
23. Zhang, L.; Si, R.; Liu, H.; Chen, N.; Wang, Q.; Adair, K.; Wang, Z.; Chen, J.; Song, Z.; Li, J.; et al. Atomic Layer Deposited Pt-Ru Dual-Metal Dimers and Identifying Their Active Sites for Hydrogen Evolution Reaction. *Nat. Commun.* **2019**, *10*, 4936. [[CrossRef](#)]
24. Zhang, J.; Huang, Q.-A.; Wang, J.; Wang, J.; Zhang, J.; Zhao, Y. Supported Dual-Atom Catalysts: Preparation, Characterization, and Potential Applications. *Chin. J. Catal.* **2020**, *41*, 783–798. [[CrossRef](#)]
25. Cai, H.; Zhang, G.; Zhang, X.; Chen, B.; Lu, Z.; Xu, H.; Gao, R.; Shi, C. Engineering the Local Coordination Environment and Density of FeN<sub>4</sub> Sites by Mn Cooperation for Electrocatalytic Oxygen Reduction. *Small* **2022**, *18*, e2200911. [[CrossRef](#)]

26. Han, X.; Ling, X.; Yu, D.; Xie, D.; Li, L.; Peng, S.; Zhong, C.; Zhao, N.; Deng, Y.; Hu, W. Atomically Dispersed Binary Co-Ni Sites in Nitrogen-Doped Hollow Carbon Nanocubes for Reversible Oxygen Reduction and Evolution. *Adv. Mater.* **2019**, *31*, e1905622. [[CrossRef](#)] [[PubMed](#)]
27. Han, X.; Zhang, T.; Chen, W.; Dong, B.; Meng, G.; Zheng, L.; Yang, C.; Sun, X.; Zhuang, Z.; Wang, D.; et al. Mn-N<sub>4</sub> Oxygen Reduction Electrocatalyst: Operando Investigation of Active Sites and High Performance in Zinc-Air Battery. *Adv. Energy Mater.* **2020**, *11*, 2002753. [[CrossRef](#)]
28. Liu, W.; Zhang, L.; Liu, X.; Liu, X.; Yang, X.; Miao, S.; Wang, W.; Wang, A.; Zhang, T. Discriminating Catalytically Active FeN<sub>x</sub> Species of Atomically Dispersed Fe-N-C Catalyst for Selective Oxidation of the C-H Bond. *J. Am. Chem. Soc.* **2017**, *139*, 10790–10798. [[CrossRef](#)]
29. Lang, L.; Shi, Y.; Wang, J.; Wang, F.; Xia, X. Hollow Core-Shell Structured Ni-Sn@C Nanoparticles: A Novel Electrocatalyst for the Hydrogen Evolution Reaction. *ACS Appl. Mater. Interfaces* **2015**, *7*, 9098–9102. [[CrossRef](#)]
30. Wang, X.X.; Cullen, D.A.; Pan, Y.T.; Hwang, S.; Wang, M.; Feng, Z.; Wang, J.; Engelhard, M.H.; Zhang, H.; He, Y.; et al. Nitrogen-Coordinated Single Cobalt Atom Catalysts for Oxygen Reduction in Proton Exchange Membrane Fuel Cells. *Adv. Mater.* **2018**, *30*, 1706758. [[CrossRef](#)]
31. Zou, L.; Wei, Y.S.; Hou, C.C.; Li, C.; Xu, Q. Single-Atom Catalysts Derived from Metal-Organic Frameworks for Electrochemical Applications. *Small* **2021**, *17*, e2004809. [[CrossRef](#)] [[PubMed](#)]
32. Cao, B.; Zeng, L.; Liu, H.; Shang, J.; Wang, L.; Lang, J.; Cao, X.; Gu, H. Synthesis of the Platinum Nanoribbons Regulated by Fluorine and Applications in Electrocatalysis. *Inorg. Chem.* **2021**, *60*, 4366–4370. [[CrossRef](#)] [[PubMed](#)]
33. Singh, B.; Sharma, V.; Gaikwad, R.P.; Fornasiero, P.; Zbořil, R.; Gawande, M.B. Single-Atom Catalysts: A Sustainable Pathway for the Advanced Catalytic Applications. *Small* **2021**, *17*, e2006473. [[CrossRef](#)] [[PubMed](#)]
34. Qu, X.; Han, Y.; Chen, Y.; Lin, J.; Li, G.; Yang, J.; Jiang, Y.; Sun, S. Stepwise Pyrolysis Treatment as An Efficient Strategy to Enhance the Stability Performance of Fe-N<sub>x</sub>/C Electrocatalyst Towards Oxygen Reduction Reaction and Proton Exchange Membrane Fuel Cell. *Appl. Catal. B* **2021**, *295*, 2101242. [[CrossRef](#)]
35. Wang, Q.; Yang, Y.; Sun, F.; Chen, G.; Wang, J.; Peng, L.; Chen, W.T.; Shang, L.; Zhao, J.; Sun-Waterhouse, D.; et al. Molten NaCl-Assisted Synthesis of Porous Fe-N-C Electrocatalysts with a High Density of Catalytically Accessible FeN<sub>4</sub> Active Sites and Outstanding Oxygen Reduction Reaction Performance. *Adv. Energy Mater.* **2021**, *11*, 2101242.
36. Li, J.; Chen, M.; Cullen, D.A.; Hwang, S.; Wang, M.; Li, B.; Liu, K.; Karakalos, S.; Lucero, M.; Zhang, H.; et al. Atomically Dispersed Manganese Catalysts for Oxygen Reduction in Proton-Exchange Membrane Fuel Cells. *Nat. Catal.* **2018**, *1*, 935–945. [[CrossRef](#)]
37. Shi, Y.; Tada, E.; Nishikata, A. Erratum: A Method for Determining the Corrosion Rate of a Metal under a Thin Electrolyte Film. *J. Electrochem. Soc.* **2017**, *164*, X10. [[CrossRef](#)]
38. Thompson, S.T.; Wilson, A.R.; Zelenay, P.; Myers, D.J.; More, K.L.; Neyerlin, K.; Papageorgopoulos, D. ElectroCat: DOE's Approach to PGM-Free Catalyst and Electrode R&D. *Solid State Ion.* **2018**, *319*, 68–76.
39. Guo, L.; Hwang, S.; Li, B.; Yang, F.; Wang, M.; Chen, M.; Yang, X.; Karakalos, S.G.; Cullen, D.; Feng, Z.; et al. Promoting Atomically Dispersed MnN<sub>4</sub> Sites via Sulfur Doping for Oxygen Reduction: Unveiling Intrinsic Activity and Degradation in Fuel Cells. *ACS Nano* **2021**, *15*, 6886–6899. [[CrossRef](#)]
40. Liu, K.; Qiao, Z.; Hwang, S.; Liu, Z.; Zhang, H.; Su, D.; Xu, H.; Wu, G.; Wang, G. Mn- and N- doped Carbon as Promising Catalysts for Oxygen Reduction Reaction: Theoretical Prediction and Experimental Validation. *Appl. Catal. B* **2019**, *243*, 195–203. [[CrossRef](#)]
41. Zhang, S.; Xue, H.; Li, W.; Sun, J.; Guo, N.; Song, T.; Dong, H.; Zhang, J.; Ge, X.; Zhang, W.; et al. Constructing Precise Coordination of Nickel Active Sites on Hierarchical Porous Carbon Framework for Superior Oxygen Reduction. *Small* **2021**, *17*, e2102125. [[CrossRef](#)]
42. Wang, D.; Liu, J.; Xi, J.; Jiang, J.; Bai, Z. Pd-Fe Dual-metal Nanoparticles Confined in the Interface of Carbon Nanotubes/N-doped Carbon for Excellent Catalytic Performance. *Appl. Surf. Sci.* **2019**, *489*, 477–484. [[CrossRef](#)]
43. Xu, J.; Elangovan, A.; Li, J.; Liu, B. Graphene-Based Dual-Metal Sites for Oxygen Reduction Reaction: A Theoretical Study. *J. Phys. Chem. C* **2021**, *125*, 2334–2344. [[CrossRef](#)]
44. Chen, Z.; Liao, X.; Sun, C.; Zhao, K.; Ye, D.; Li, J.; Wu, G.; Fang, J.; Zhao, H.; Zhang, J. Enhanced Performance of Atomically Dispersed Dual-Site Fe-Mn Electrocatalysts through Cascade Reaction Mechanism. *Appl. Catal. B* **2021**, *288*, 120021. [[CrossRef](#)]
45. Chen, D.; Li, G.; Chen, X.; Zhang, Q.; Sui, J.; Li, C.; Zhang, Y.; Hu, J.; Yu, J.; Yu, L.; et al. Developing Nitrogen and Co/Fe/Ni Multi-Doped Carbon Nanotubes as High-Performance Bifunctional Catalyst for Rechargeable Zinc-Air Battery. *J. Colloid. Interface Sci.* **2021**, *593*, 204–213. [[CrossRef](#)] [[PubMed](#)]
46. Buchwalter, P.; Rose, J.; Braunstein, P. Multimetallic Catalysis Based on Heterometallic Complexes and Clusters. *Chem. Rev.* **2015**, *115*, 28–126. [[CrossRef](#)] [[PubMed](#)]
47. Hunter, M.A.; Fischer, J.M.T.A.; Yuan, Q.; Hankel, M.; Searles, D.J. Searles, Evaluating the Catalytic Efficiency of Paired, Single-Atom Catalysts for the Oxygen Reduction Reaction. *ACS Catal.* **2019**, *9*, 7660–7667. [[CrossRef](#)]

48. Han, Y.; Li, Q.K.; Ye, K.; Luo, Y.; Jiang, J.; Zhang, G. Impact of Active Site Density on Oxygen Reduction Reactions Using Monodispersed Fe-N-C Single-Atom Catalysts. *ACS Appl. Mater. Interfaces* **2020**, *12*, 15271–15278. [[CrossRef](#)]
49. Fan, L.; Liu, P.F.; Yan, X.; Gu, L.; Yang, Z.Z.; Yang, H.G.; Qiu, S.; Yao, X. Atomically Isolated Nickel Species Anchored on Graphitized Carbon for Efficient Hydrogen Evolution Electrocatalysis. *Nat. Commun.* **2016**, *7*, 10667. [[CrossRef](#)]

**Disclaimer/Publisher's Note:** The statements, opinions and data contained in all publications are solely those of the individual author(s) and contributor(s) and not of MDPI and/or the editor(s). MDPI and/or the editor(s) disclaim responsibility for any injury to people or property resulting from any ideas, methods, instructions or products referred to in the content.